



High-throughput 3DRA segmentation of brain vasculature and aneurysms using deep learning



Fengming Lin^a, Yan Xia^{a,*}, Shuang Song^a, Nishant Ravikumar^a, Alejandro F. Frangi^{a,b,c,d}

^a Centre for Computational Imaging and Simulation Technologies in Biomedicine (CISTIB), The University of Leeds, Leeds LS2 9JT, UK

^b Leeds Institute for Cardiovascular and Metabolic Medicine (LICAMM), School of Medicine, University of Leeds, Leeds LS2 9JT, UK

^c Medical Imaging Research Center (MIRC), Cardiovascular Science and Electronic Engineering Departments, KU Leuven, Leuven, Belgium

^d Alan Turing Institute, London, UK

ARTICLE INFO

Article history:

Received 1 August 2022

Revised 10 January 2023

Accepted 13 January 2023

Keywords:

Image segmentation

Patch-based learning

Majority voting

Class imbalance

ABSTRACT

Background and Objectives: Automatic segmentation of the cerebral vasculature and aneurysms facilitates incidental detection of aneurysms. The assessment of aneurysm rupture risk assists with pre-operative treatment planning and enables in-silico investigation of cerebral hemodynamics within and in the vicinity of aneurysms. However, ensuring precise and robust segmentation of cerebral vessels and aneurysms in neuroimaging modalities such as three-dimensional rotational angiography (3DRA) is challenging. The vasculature constitutes a small proportion of the image volume, resulting in a large class imbalance (relative to surrounding brain tissue). Additionally, aneurysms and vessels have similar image/appearance characteristics, making it challenging to distinguish the aneurysm sac from the vessel lumen.

Methods: We propose a novel multi-class convolutional neural network to tackle these challenges and facilitate the automatic segmentation of cerebral vessels and aneurysms in 3DRA images. The proposed model is trained and evaluated on an internal multi-center dataset and an external publicly available challenge dataset.

Results: On the internal clinical dataset, our method consistently outperformed several state-of-the-art approaches for vessel and aneurysm segmentation, achieving an average Dice score of 0.81 (0.15 higher than nnUNet) and an average surface-to-surface error of 0.20 mm (less than the in-plane resolution (0.35 mm/pixel)) for aneurysm segmentation; and an average Dice score of 0.91 and average surface-to-surface error of 0.25 mm for vessel segmentation. In 223 cases of a clinical dataset, our method accurately segmented 190 aneurysm cases.

Conclusions: The proposed approach can help address class imbalance problems and inter-class interference problems in multi-class segmentation. Besides, this method performs consistently on clinical datasets from four different sources and the generated results are qualified for hemodynamic simulation. Code available at <https://github.com/cistib/vessel-aneurysm-segmentation>.

© 2023 Published by Elsevier B.V.

1. Introduction

Cerebral aneurysms are pathological protrusions of cerebral arterial walls (see Fig. 1, for example), and their rupture is the leading cause of subarachnoid hemorrhage in patients. Three-dimensional X-ray rotational angiography (3DRA) [4,35,36] imaging is commonly used to visualize and characterize cerebral vessels and aneurysms through the reconstruction of tomographic slices of a region of interest like computed tomography angiography (CTA),

using single-plane radiographic equipment [2,3]. In contrast with 3D magnetic resonance angiography (MRA) imaging and CTA, 3DRA provides images of higher spatial resolution and improved soft-tissue contrast [32–34], capturing fine vascular structures and enabling precise characterization of aneurysm morphology.

An accurate, automated, and reproducible cerebral vessel and aneurysm segmentation technique would facilitate various computational imaging and clinical applications. Segmentation of cerebrovasculature has found its use in pre-operative planning of invasive procedures [37,39], delivering image-guided therapies/treatments [40], and assessing cerebral hemodynamics through computational fluid dynamics (CFD) simulations [41]. Similarly, detection and segmentation of cerebral aneurysms are

* Corresponding author.

E-mail address: y.xia@leeds.ac.uk (Y. Xia).



Fig. 1. From left to right: 2D slice from a reconstructed 3DRA image; the maximum intensity projection (MIP) of the 3DRA image; and a 3D simulation-ready mesh of a cerebral aneurysm (blue) and the major vessels (white) in its vicinity reconstructed from its corresponding main vessel segmentation. (For interpretation of the references to colour in this figure legend, the reader is referred to the web version of this article.)

valuable as they facilitate incidental identification and quantitative characterization of aneurysm morphology [42,48]. The latter is especially useful as previous studies have shown that the size and shape of a cerebral aneurysm are essential biomarkers for evaluating rupture risk [38]. Precise characterization of aneurysm location and morphology is necessary for selecting a suitable/approved treatment strategy, pre-operative intervention planning, and post-operative assessment and monitoring. While cerebral aneurysms and their surrounding vessels can be detected and segmented manually, this process is time-consuming due to the high dimensionality of 3D image volumes and is subject to inter- and intra-observer variability. If the computer-assisted model can automatically detect the location of the aneurysm and characterize its morphological properties such as neck diameter, aneurysm size, etc., all of these characteristics can support the clinical decision-making process. For instance, depending on the size and location of the aneurysm, the clinician would either use coils or flow diverters to treat the aneurysm. Similarly, to decide the type of medical device for treating the aneurysm, the clinician relies on the information on whether there is a bifurcation around the aneurysm. On the one hand, the direct clinical needs involve automatically characterizing the location and morphological properties of the aneurysm which could inform the best course of treatment for the aneurysm. On the other hand, to motivate clinical needs, *in-silico trials* [43] can help identify the best operational regimes for the use of certain devices and better inform the safety and efficacy of medical devices in clinical trials. In order to be able to scale up *in-silico trials* to large-scale, both qualified vessel and aneurysm segmentation are required to derive accurate geometrical and computational models.

Several previous studies have proposed automatic and semi-automatic techniques for cerebral vessel and aneurysm segmentation in 3D imaging modalities such as MRA, CTA, and 3DRA. While early work in the field relied on classical techniques such as geodesic active regions for segmenting vessels and aneurysms [44–46], recent approaches have focused on data-driven supervised learning-based methods due to the tremendous success of convolutional neural networks (CNNs) at detecting and segmenting objects/regions in images. As in several other domains, the segmentation performance afforded by deep learning-based approaches for cerebral vessels and aneurysms far exceeds that of classical approaches. For example, in a recent study [17], the authors proposed DeepVesselNet, a CNN designed to segment cerebral vessels in MRA images. Here, 2D orthogonal cross-hair filters (convolutions) were used to preserve details of fine vascular structures in the learned features while incorporating 3D contextual information. As vessels constitute a small fraction of the overall image volume, the segmentation task suffers from a significant class imbalance between the foreground (vessel) and background

(surrounding brain tissue) classes. This was addressed by training DeepVesselNet with a class-balanced cross-entropy loss function that minimizes the false-positive rate. Similarly, to incorporate 3D contextual information and improve the accuracy of segmenting fine vessels [12] in digital subtraction angiography, Patel et al., [13] used DeepMedic, a powerful segmentation approach proposed in a previous study [10]. To improve the performance of deep learning on small object segmentation and obtain annotated training data at a rapid pace, Vessel-CAPTCHA [50] proposes a novel annotation-efficient deep learning vessel segmentation framework. The framework only requires weak patch-level labels to discriminate between the vessel and non-vessel 2D patches in the training set. This framework can effectively segment vessels including both main and fine branches. Unlike the original U-Net architecture [14], DeepMedic is a 3D CNN with two parallel encoder pathways that learn features at different image resolutions to capture contextual information while keeping the computational cost low. 3D image patches centered at the same location in the image are used as inputs to the two pathways. The image is downsampled to a third of its original size for the second pathway. Several U-Net based approaches have been proposed for segmenting cerebral vessels and aneurysms [6–9]. The method proposed by Livne et al. [6] is trained to segment cerebral vessels using 2D patches extracted from MRA images [11] with a U-Net. The method proposed by Shahzad et al. [9] segments ruptured intracranial aneurysms resulting in subarachnoid hemorrhage in CTA images using DeepMedic. Zhou et al. [15] proposed U-Net++ as a new framework for image segmentation to further improve segmentation performance. The redesigned skip connections in U-Net++ aggregate features across multiple scales within decoder sub-networks, leading to a highly flexible feature fusion scheme. Attention modules have been widely used in vessel segmentation networks to weigh the importance of relevant but under-represented structures/features [26–29]. However, stand-alone segmentation networks trained and applied to imaging data without using appropriate pre, and post-processing steps typically lack robustness when segmenting fine structures (such as vessels and aneurysms) in the presence of significant class imbalance and variability in image appearance and soft-tissue contrast (typical of imaging data acquired across multiple centers). Therefore, to facilitate robust segmentation of diverse imaging data with imbalanced classes, Isensee et al. [1] proposed nnUNet, which can automatically configure itself, including pre-processing, network architecture, and training and post-processing for any new task in the biomedical domain. The nnUNet improves the robustness of the model by learning fixed, rule-based and empirical parameters.

The methods discussed thus far achieved state-of-the-art segmentation performance for cerebrovascular structures. However,

several challenges remain to enable precise and robust characterization of cerebral vessels and aneurysms in 3D, namely, effectively dealing with the severe class imbalance, the difficulty of distinguishing between the aneurysm and vessel lumen, and the lack of a robust deep learning framework for segmenting cerebral vessels and aneurysms for multi-center studies. Firstly, the aneurysm region often constitutes less than 1% of the overall image volume. The features extracted from the small regions such as fine vessels and aneurysms may not be effectively propagated through a series of convolutional and up-/down-sampling layers by conventional CNN-based networks. Secondly, vessel interference is the main reason for over-segmentation due to the similarity of closed vessels in patch boundaries to aneurysms in morphology. Last, multi-center imaging data varies considerably in image appearance and spatial resolution due to different scanners and image acquisition protocols across different institutions. All these factors make precise segmentation of cerebral vessels and aneurysms challenging. Addressing these challenges is the main focus of this study and here are the contributions:

1) A dual-class segmentation network is proposed for the automatic segmentation of cerebral vessels and aneurysms in 3DRA images. To deal with the class imbalance inherent in such a segmentation task, especially for aneurysms, we proposed a cascaded transformer block at the end of the encoder to highlight aneurysm features. Multi-view blocks are designed to receive continuous features in a lower feature dimension. Learnable downsample blocks are proposed at the end of every encoder block to prevent small features from being washed out during down-sampling. Wide blocks are designed to extract high-level features in multi-dimensions.

2) For the inter-class interference challenge, we designed the multi-class network with weighted Dice loss and set aneurysms as a subclass of vessels. The semantic guidance from vessel features reduces the interference of brain tissue and skull with aneurysms and can significantly improve aneurysm segmentation performance.

3) To further enhance the aneurysm segmentation performance, we designed a post-processing pipeline including majority voting and self-refinement which can predict accurate aneurysm localization and boundary.

4) For hemodynamics simulation analysis, to the best of our knowledge, previous methods have segmented vessels or aneurysms individually and most experiments have been validated on image-based evaluation metrics like Dice. Whether the independent outputs of these segmentation methods are suitable for vessel and aneurysm simulation is still unknown. Our method allows the simultaneous segmentation of shape-consistent vessels and aneurysms. More importantly, after generating the mesh from the image-based output, a mesh-based surface-to-surface error evaluation was performed to verify that the output is suitable for simulation (surface-to-surface error 0.20 mm for aneurysm segmentation and 0.25 mm for vessel segmentation, less than the in-plane resolution 0.35 mm/pixel). The automatic segmentation pipeline can bridge the gap between clinical data and hemodynamic simulation input.

We comprehensively evaluated the proposed approach across two 3DRA datasets: an in-house multi-center @neurIS dataset [18] and a publicly available cerebral aneurysm detection and analysis dataset (CADA) [19].

2. Materials and methods

This section describes the 3D multi-class cerebral vessel and aneurysm segmentation network proposed in this study and the overall pipeline developed to ensure robust and reproducible segmentation performance. The proposed multi-class CNN incorpo-

rates several architectural components dedicated to preserving fine structural details in-plane across multiple orthogonal planes, and ensures consistency in 3D for the vascular structures of interest. The proposed pipeline comprises three steps: pre-processing, multi-class segmentation, and post-processing in Fig. 2. Details of each step of the pipeline and the architectural components developed for the multi-class segmentation network are discussed in subsequent subsections.

2.1. Step1: Pre-processing

The first step in our segmentation pipeline focuses on processing the original 3DRA image volumes to generate 3D image patches suitable for training the multi-class segmentation network. Before extracting patches from the image volumes, we use a sequence of operations to reduce the variability across patients' images and stabilize subsequent segmentation network training. As the spatial resolution varies across patients' images in the @neurIST database, we standardized the resolution of all image volumes by resampling them to a fixed voxel size of $0.35 \times 0.35 \times 0.35$ mm. We also applied histogram equalization to the resampled image volumes to reduce differences in tissue contrast across patients' images. Then, we normalized voxel intensities in all images to [0,1]. Vascular structures are only partially labeled within the @neurIST dataset, with ground-truth segmentations available just for the major cerebral arteries and their branches in the vicinity of the aneurysm. Hence, we cropped each image volume using a bounding box encapsulating the labeled structures to reduce label noise/confounding information when training the segmentation network. Finally, we extracted 3D patches of size $64 \times 64 \times 64$ voxels from the cropped volumes, discarding all patches that had no associated labels for the vessels or aneurysm, and used the remaining patches for training our segmentation network.

2.2. Step2: Multi-class segmentation network

The backbone of our multi-class segmentation network's architecture is U-Net++ [15], a deeply supervised encoder-decoder network with nested dense connections across convolution blocks nestled between the encoder and decoder paths (as illustrated in Fig. 2). The nested dense skip pathways help aggregate multiscale features at each convolution block in the decoder from all convolution blocks at the same resolution level or below (relative to the former) in the encoder. These dense connections help alleviate the restrictive behavior of skip connections (allowing only for the same-scale fusion of learned features) used in the original U-Net architecture and its variants. They enable rich semantic multiscale features from different encoder blocks to be used by each decoder block to generate segmentations. Additionally, we propose several additional feature extraction modules (discussed in subsequent sections) integrated into this backbone U-Net++ architecture to increase the network's sensitivity to detect vessels and aneurysms.

2.2.1. Cascaded transformer

Cerebral vessels and aneurysms constitute less than 6% of the overall image volume in 3DRA images [47]. This leads to a significant class imbalance between the foreground (vessels and aneurysms) and background (surrounding tissues) classes. We designed a cascaded transformer block to address this challenge, which adaptively increases the network's attention on vessels and aneurysms [16,31]. As shown in Fig. 3., we first exploited this module at the end of the encoder to integrate local features with their global dependencies along the spatial and channel dimensions in parallel paths. The spatial attention module on the top left selectively highlights the locations that comprise vessels and aneurysms

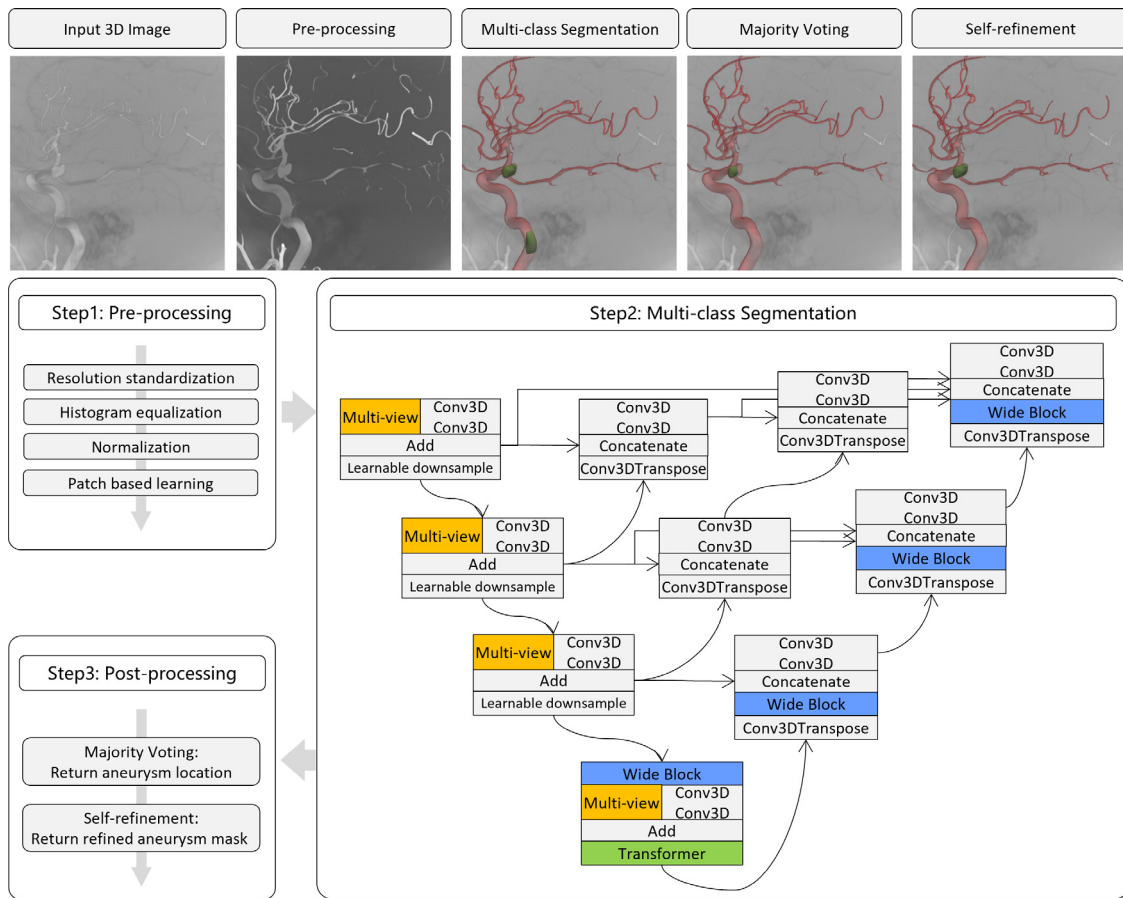


Fig. 2. Schematic of the proposed cerebral vessels and aneurysm segmentation pipeline comprising three steps. Step 1: shows the pre-processing operations applied to the original 3DRA images; Step 2: shows the architecture of the proposed multi-class CNN-based segmentation model; Step 3: shows the post-processing operations applied to segmented images based on majority voting and self-refinement.

by a weighted sum of the features from all locations. Meanwhile, the channel attention module on the top right enhances the interdependence between different channels through a sequence of permutation and dot product operations acting channel-wise on the input feature maps. Then, we exploited three multi-head attention modules cascaded with multilayer perception (MLP) in latent space to further learn features with a wider spatial context. Since the feature order in latent space is learned by the model rather than by spatial position, we removed the position embedding layer here to reduce artificial interference and provide more room for learning. Finally, we add the features from different attention stages, increasing training stability and the weight of key features specific to vessels and aneurysms to enhance overall segmentation performance.

2.2.2. Multi-view block

Learning representative features of fine vessels is challenging as they may be as few as two pixels in diameter in Fig. 13. Because of the presence of noise points in the low-level features, convolution with a kernel size three has difficulty distinguishing noise from such subtle features with a diameter of less than three. These noise-like features are either filtered out or over-enhanced by using only small kernel 3D convolution filters. But in large receptive field, this continuous and uniformly slender feature will be completely different from the noise point feature. We propose a multi-view convolution block composed of three branches to extract 2D features in the larger receptive field along orthogonal planes of the 3D image volume to tackle this challenge. This enables feature learning and orthogonal views, which are subsequently aggregated,

to highlight the slender features specific to fine vessels. This represents finer vascular structures than conventional 3D convolutions. Besides, we are also interested in preserving the 3D structure and morphology of vessels and aneurysms, which is somewhat lost using just 2D orthogonal convolutions. Hence, we also use a 3D convolution layer alongside each multi-view block in our network, and add the features learned by the former and latter. This combination of the multi-view block and a 3D convolution layer ensures that 3D contextual features are learned and aggregated with detailed features of fine vascular structures. The structure of the multi-view block is shown in Fig. 4.

2.2.3. Learnable downsample block

Down-sampling of learned feature maps through pooling operations is essential in CNNs to increase the receptive field size of the network and enable learning of hierarchical features while keeping model complexity (i.e. the number of learnable parameters) reasonable to reduce overfitting and ensure computational tractability. During down-sampling, weak features of small vessels and aneurysms are easily ignored/lost if standard pooling operations are used (e.g. max-pooling). We designed a learnable downsample block to retain weak features to compensate for this. This block halves the size of the input feature maps along three parallel branches comprising two stridden convolution branches and a max-pooling branch, as illustrated in Fig. 5 (left). These three branches dissociate the spatial and channel information through a 3D convolution layer (with a kernel size of 3) for the former and three parallel 2D convolutional layers (multi-view block) of factorized asymmetric 3D convolutions for the latter (as shown in Fig. 5).

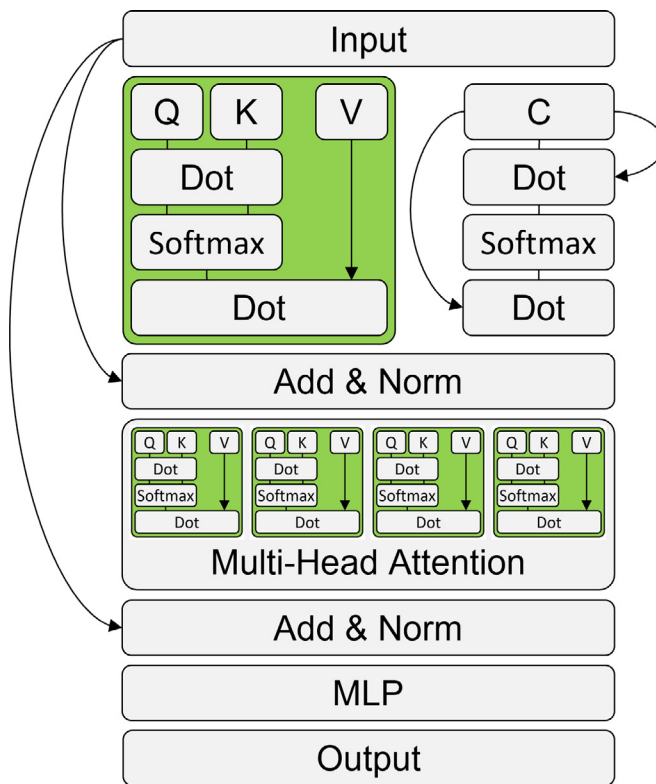


Fig. 3. Transformer block. Increased attention to aneurysms and fine vessels.

This enables effective learning of spatial and channel-wise features alongside down-sampling of the feature maps in each individual path. The max-pooling path downsamples the input feature maps and aggregates them across channels using a 3D convolution layer with a kernel size of one. The resulting feature maps from all three branches are subsequently concatenated, resulting in downsampled

feature maps that have preserved weak features across multiple scales and dimensions.

2.2.4. Wide block

To further increase the receptive field size of the network, with a limited increase in model complexity, and learn features with a wider spatial context, we designed the wide block. This module comprises three branches in Fig. 5 (right). One branch aggregates the feature maps across channels and learns local features with a 3D convolution of kernel size three. The other two branches utilize asymmetric 3D convolutions applied in parallel and serially with a large kernel size to learn multiscale features along all dimensions. The resulting feature maps from each branch are finally concatenated and provided as input to subsequent network layers.

2.2.5. Loss function

The aneurysm regions account for only a small part of the brain image, and a critical imbalance exists in the distribution of the positive and negative samples. Thus, following the generalized dice loss proposed in [49], in this work, we used the weighted dice loss (Eq. (1)) [25] that weights inversely proportional to labels area, in order to better predict labels with general small regions, i.e., the aneurysms in our case. w_a and w_v are the weights of the aneurysm and vessel volume in Eq. (2). Dice is calculated in Eq. (3). Because of the class imbalance issue, we compensated for this by multiplying the Dice of aneurysm segmentation whose proportion is small by the larger weights and multiplying the vessel segmentation whose proportion is big by the smaller weights.

$$\text{Loss} = w_v * \text{Dice}_a + w_a * \text{Dice}_v \quad (1)$$

$$w_a = \frac{V_a}{V_a + V_v}, w_v = \frac{V_v}{V_a + V_v} \quad (2)$$

2.3. Post-processing

2.3.1. Majority voting

The multi-class segmentation network processes patch data. In the segmentation result of a single patch, a vessel near the patch

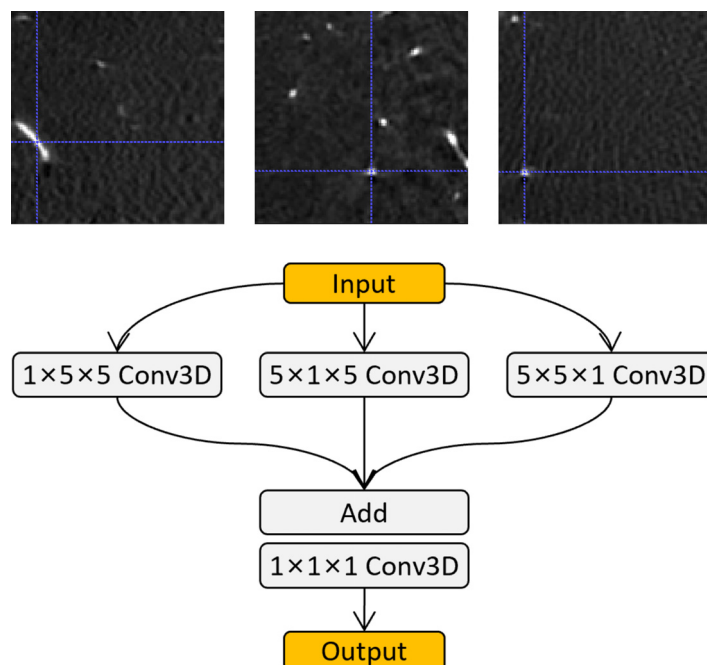


Fig. 4. Multi-view block. Extract features from three orthogonal views using 2D convolutions in large kernels. The fine vessel feature is not obvious in the second and third views, but the slender feature is easily captured in the first view.

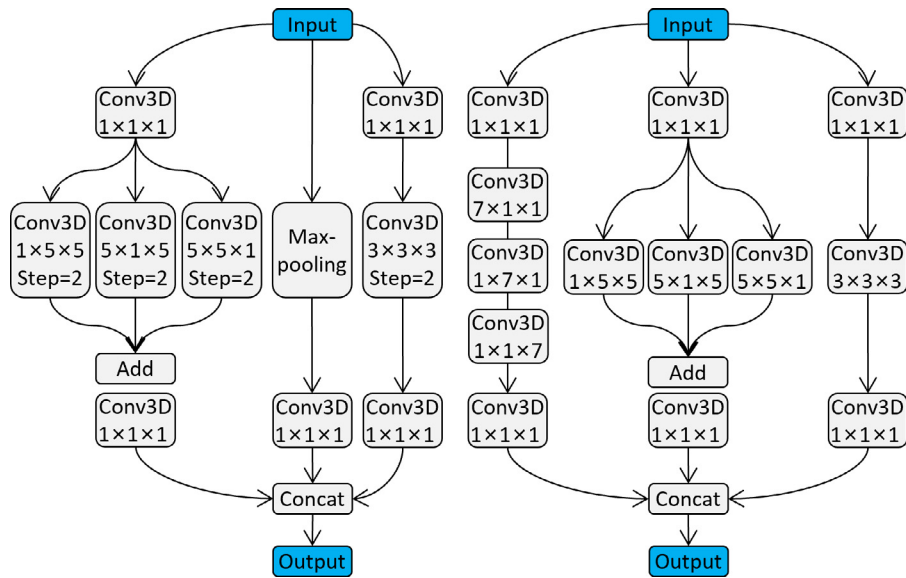


Fig. 5. Learnable downsample block (left) and wide block (right).

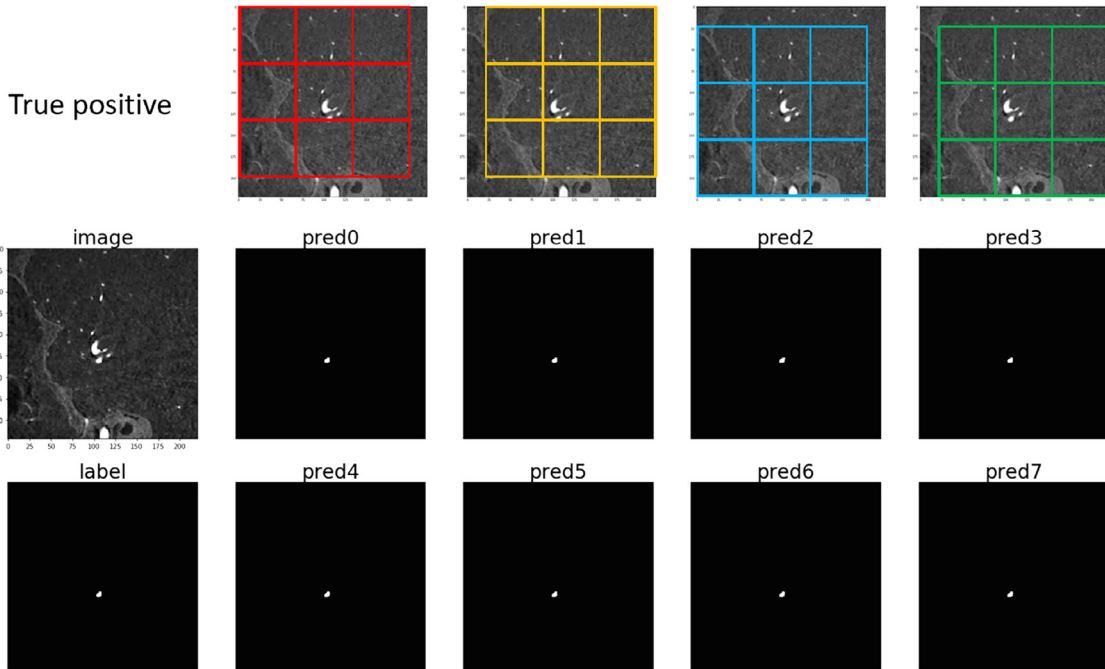


Fig. 6. Patch grouping example and inference results. 2D image have four patch groups, 3D image will have eight patch groups. The different colors represent the different patch groups. The label shows here is an aneurysm and the prediction of eight different groups is correct.

edge has a closed geometry and is therefore incorrectly identified as an aneurysm. After ensembling the predictions of patches together, there will be over-segmentation of aneurysms like the fourth column of Fig. 2. As visualized in Figs. 6 and 7, the 2D image is divided into four groups of patches represented in red, yellow, green and blue boxes. Similarly, the 3D image is divided into eight groups of patches. Each group of patches is fed into the multi-class model for prediction. For true aneurysms in 6, all eight groups had positive prediction results (eight votes). For fake aneurysms (vessels near the patch edge mentioned above) in Fig. 7, only four groups (pred 2, 4, 6, 7) had positive prediction results (four votes), the remaining four groups (pred 0, 1, 3, 5) did not predict the controversial area to be an aneurysm. Therefore, after ensembling the results of eight groups, we keep only the predicted area with the highest number of votes and use this area as the aneurysm predic-

tion of majority voting. The proposed approach decomposes each 3DRA image volume into eight groups of patches and uses these to train the multi-class segmentation network. The starting points of the eight groups are the eight vertices of the 3D image after zero-padding, which is to ensure the eight groups do not overlap completely. Patch-based learning allows semantic features to be learned from the 3DRA images in their native resolution with a limited degree of down-sampling throughout the network, not afforded by methods that learn features directly from the original image volumes due to GPU memory constraints.

2.3.2. Self-refinement

The fourth column of Fig. 2 shows that the aneurysm may still be inaccurately over-/undersegmented. Therefore, we refine the segmentation results by selecting one patch centered on the

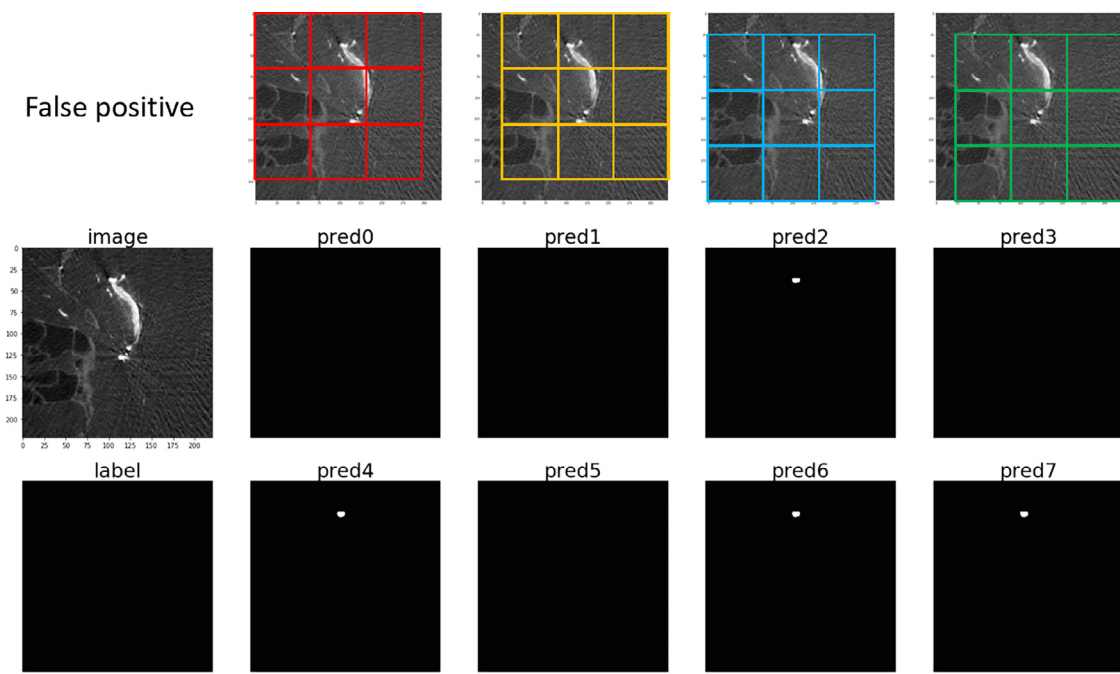


Fig. 7. Patch grouping example and inference results. The label shows there is no aneurysm. The predictions of pred0, 1, 3, and five are correct, and pred2, 4, 6, and seven are incorrect, which will cause over-segmentation.

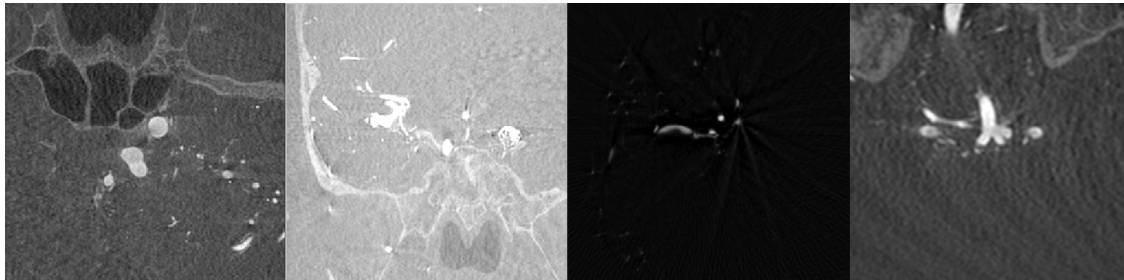


Fig. 8. Examples of images collected in the @neurIST dataset: 2D visualization of data from different four sources showed great differences in pixel distribution and aneurysm size.

aneurysm prediction (after majority voting) and feeding this patch into the multi-class model to predict the aneurysm's shape. If there are multiple independent aneurysms, patches will also be selected multiple times. During this process, the predictions close to the edge of the patch are ignored to prevent interference from vessels at the edges here. Finally, we can obtain aneurysm predictions with correct locations and accurate boundaries in the fifth column of Fig. 2.

By combining majority voting with self-refinement, we can prevent vessels at the edge of the patch from being predicted as aneurysms, effectively suppressing aneurysm over-segmentation.

3. Experimental setup

3.1. Datasets

The proposed method is trained and validated on 3DRA images from 223 patients acquired from the @neurIST project [18]. These images were acquired across four different centers with different scanners and imaging protocols. There are significant variations in image appearance and resolution across image data from different centers, as shown in Fig. 8. Image data from the @neurIST database were split patient-wise into training, validation, and test sets using a ratio of 7 : 1 : 2, respectively, and five-fold cross-validation experiments were conducted to thoroughly evaluate the segmen-

tation performance of the proposed approach and the state-of-the-art methods. The test sets in different cross-validation experiments traverse the entire data set. We also trained and evaluated our approach on a publicly available dataset, CADA [19], which comprises computerized tomography (CT) images of patients with cerebral aneurysms. These images were acquired as part of the Cerebral Aneurysm Detection and Analysis challenge, hosted at the international conference on medical image computing and computer-assisted interventions in 2020. The training data released as part of the CADA challenge comprised 109 3DRA images with 127 annotated aneurysms. We also split the labeled data into training, validation, and test sets by patient in a 7 : 1 : 2 ratio. When preparing the training data, we randomly extracted 3D patches around the aneurysm. Negative patches that did not contain aneurysms were not selected for training. When training the segmentation model, there were 904 patches extracted from the cropped volumes, with 716 patches being used as the training set and the rest patches being used as the validation set to monitor the training process. In addition, we applied data augmentation for these patches including left and right 90-degree rotation.

3.2. Network training

The proposed multi-class segmentation network was trained using the Adam optimizer [24] with a learning rate of 0.0003.

Table 1

Comparison of model complexity in terms of model parameters and training time/epoch between the proposed method and the benchmark networks.

Model complexity	Total params	Training time
U-Net+	1,857,939	78 s/epoch
Dual Attention Net	1,633,747	60 s/epoch
DeepVesselNet	1,608,147	57 s/epoch
Vessel-CAPTCHA	16,337,666	161 s/epoch
Ours	16,812,195	182 s/epoch

The model converged after ten epochs, and the validation loss was minimized around 30 epochs. All experiments were conducted on an NVIDIA 1080Ti GPU with 11 GB memory. The batch size was kept consistent across all experiments and was set to four. The best model is chosen according to the validation loss. We trained the network of Step2 in Fig. 2 with the above setting and shared the best weight to majority voting and self-refinement. Table 1 provides the comparison of model complexity in terms of model parameters and training time/epoch, between the proposed method and the benchmarked networks. Table 2 shows the hyper-parameter configurations for the benchmarked networks and our method. The loss functions of UNet, Dual Attention Net, UNet++, and 3DResUNet in benchmark methods are consistent with the proposed method, i.e., the weighted dice loss. The loss function of DeepVesselNet and nnUNet is Dice loss + CrossEntropy. We kept their original loss functions since DeepVesselNet and nnUNet are self-contained, highly encapsulated frameworks with dedicated pre-processing and post-processing strategies, and changing their loss functions may affect their overall performance.

3.3. Evaluation metrics

The proposed multi-class segmentation network is used to segment both cerebral vessels and aneurysms, denoted as y_{pred} . Several evaluation metrics are used to evaluate the similarity of the masks predicted for vessels and aneurysms individually regarding ground-truth masks (denoted as y_{true}). These include the Dice (or F_1) score, Jaccard (JAC) index, and the volume similarity (VS) index.

The Dice similarity index [30] measures overlap between y_{pred} and y_{true} and is calculated:

$$Dice = \frac{2 \times TP}{FP + 2 \times TP + FN}. \quad (3)$$

The Jaccard index [30] is computed as the intersection over the union of two sets and measures the similarity and diversity between two sets. It is computed:

$$JAC = \frac{TP}{FP + TP + FN}. \quad (4)$$

The VS index [30] measures the similarity between segmented regions of interest volumes in the predicted and ground-truth masks. It represents the absolute volume difference divided by the

sum of the compared volumes.

$$VS = 1 - \frac{abs(FN - FP)}{FP + 2 \times TP + FN}. \quad (5)$$

The surface-to-surface distance error [23] metrics estimate the error between the ground-truth surfaces S , and the segmentation prediction surfaces S' . The distance between a point p_i on surface S and the surface S' is given by the minimum of the Euclidean norm. And we compare the similarity between the predicted and ground-truth vessel and aneurysm geometries by generating surface mesh-based representations of these structures from their corresponding masks.

$$d(p_i, S') = \min_{p' \in S'} \|p_i - p'\|_2 \quad (6)$$

Doing this for all N points in the ground-truth surface S gives the average surface-to-surface distance error:

$$d(S, S') = \frac{1}{N} \sum_N^i d(p_i, S') \quad (7)$$

As highlighted, the ground-truth masks available for the @neurIST dataset are only partially labeled, i.e. vessel masks cover only the major artery branches near the aneurysm rather than the entire vascular tree visible within the 3DRA image field-of-view. On the other hand, as our segmentation framework is trained patch-wise to retain fine vascular details, during inference, our approach can segment the entire vascular tree using the learned representations for identifying vascular structures within the image volume. This results in a large proportion of correctly identified pixels as vessels, for which no ground-truth labels exist. Thus, the surface-to-surface distance may be more appropriate in this scenario as it only computes the distance errors for the GT labeled region.

Across all comparative evaluations conducted comparing the proposed segmentation framework with state-of-the-art approaches and in the ablation study evaluating the impact of each module included in the proposed multi-class network, we assess the statistical significance of the obtained segmentation results using paired-sample Student's t-tests.

4. Results

4.1. Visual comparison

Figure 9 illustrates the 3D renderings of obtained segmentation results captured in the entire field of view in 3DRA images. These data samples were randomly selected from different data collection centers. As can be seen, the proposed method can capture much more abundant vascular structures in the images, which were mislabelled as the background in manual annotations. The segmented results preserve the continuity and topology of the vascular trees and are visually comparable to the annotated regions.

The surface meshes generated using the vessel and aneurysm segmentations predicted at different stages of our segmentation

Table 2

Summary of the hyper-parameter configurations for the benchmarked networks and the proposed method.

Hyper-parameters	U-Net+	Dual Attention Net	DeepVesselNet	3DResUNet	Vessel-CAPTCHA	nnUnet	Ours
Optimizer	Adam	Adam	Adam	Adam	Adam	SGD	Adam
Learning Rate	0.0003	0.0003	0.0003	0.0003	0.0003	0.001 Decay	0.0003
Epochs	40	40	40	40	40	200	40
Batch Size	4	4	4	4	64	4	4
Patch Size	64	64	64	64	64	64	64
Dimension	3D	3D	3D	3D	2D	3D	3D

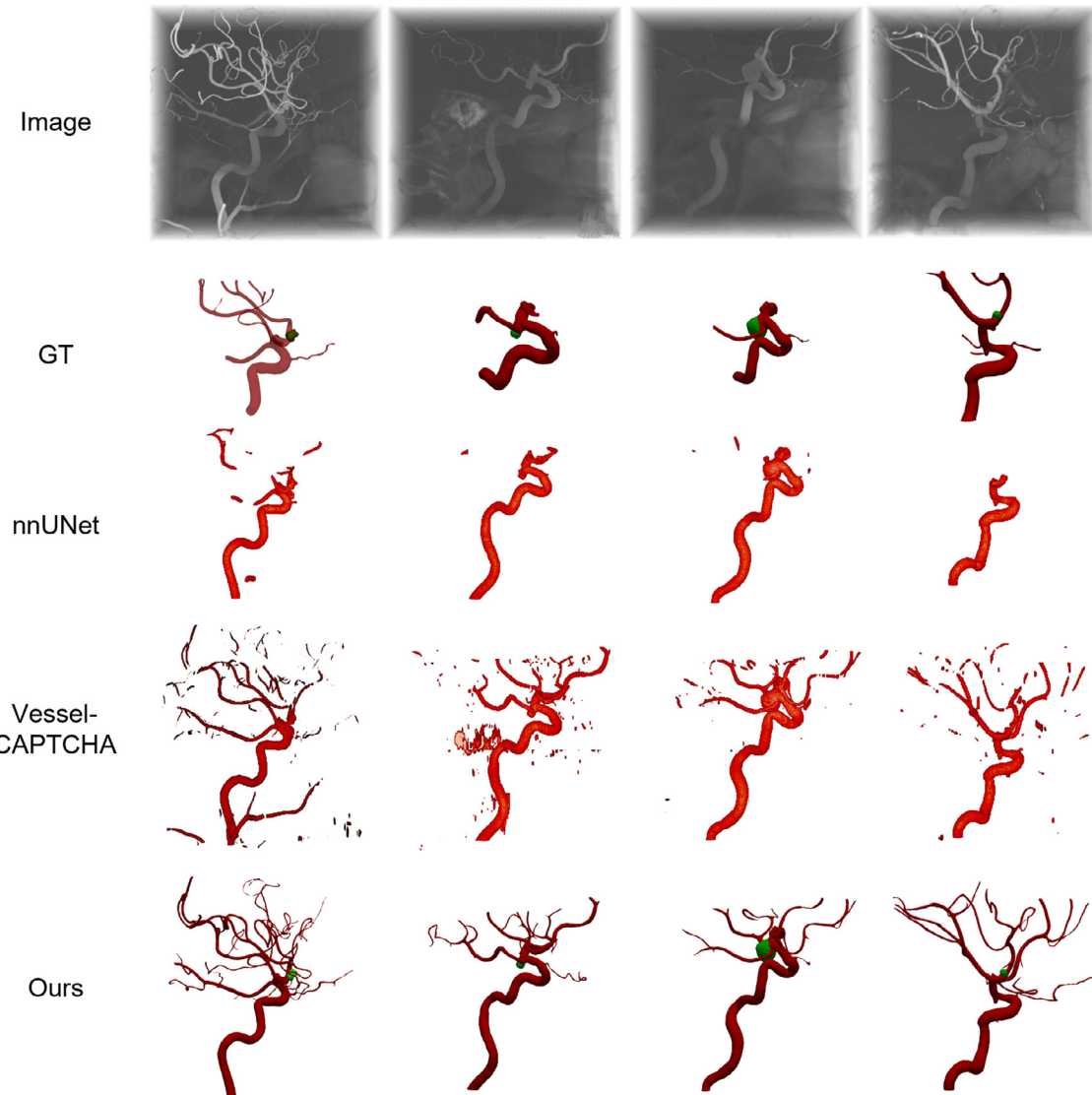


Fig. 9. 3D renderings of obtained segmentations. These data samples were selected from different centers.

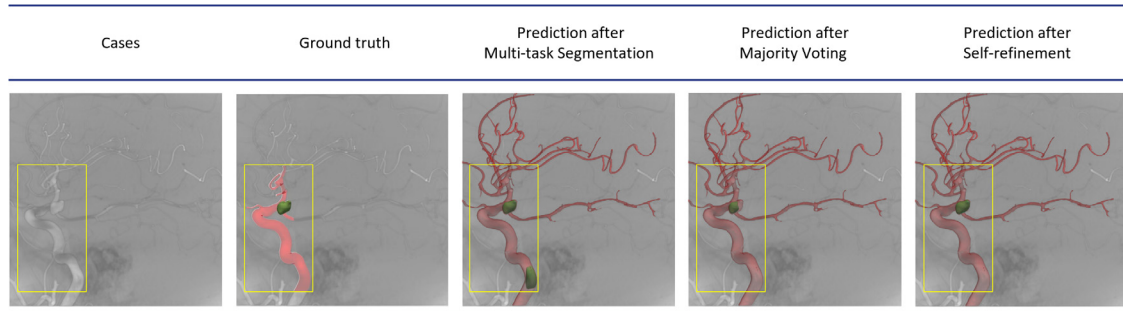


Fig. 10. 3D renderings of obtained segmentations after different steps.

pipeline are shown in **Fig. 10**. These figures demonstrate the utility of the proposed post-processing steps to suppress false-positive predictions for the aneurysm and refine the same. Cropped vessels share similarities in topology and appearance with aneurysms near patch boundaries. Therefore, initial segmentation using the proposed multi-class segmentation network (step 2 in **Fig. 2**) is prone to incorrectly labeling tortuous vessels and vessels near patch boundaries as aneurysms (example in the third column of

Fig. 10). These false-positive predictions for aneurysms are artifacts of patch-based learning due to the limited spatial context available to the network during feature learning and can be effectively reduced using majority voting (described as part of the post-processing step earlier in **Section 2.3-C**). The resulting aneurysm segmentation following the suppression of false positives by majority voting (see the fourth column of **Fig. 10**) is used to provide aneurysm location and extract patches in the neighborhood, which

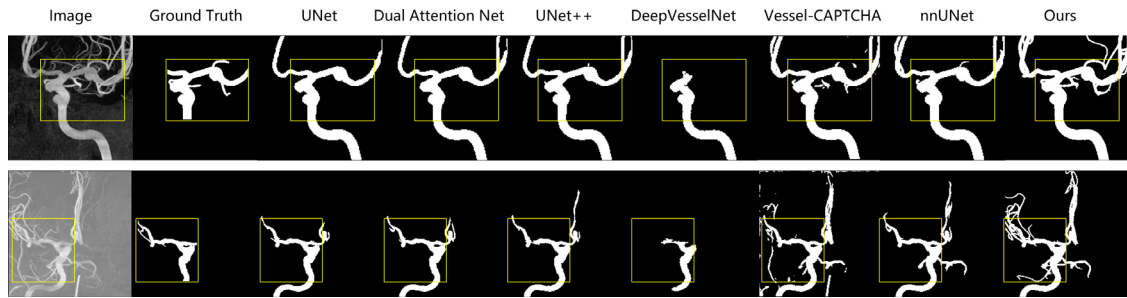


Fig. 11. Maximum intensity projection for vessel segmentation. The yellow box is the golden standard area, where all quantitative evaluations are carried out. Our method captures more fine vascular structures than its state-of-the-art counterparts. (For interpretation of the references to colour in this figure legend, the reader is referred to the web version of this article.)

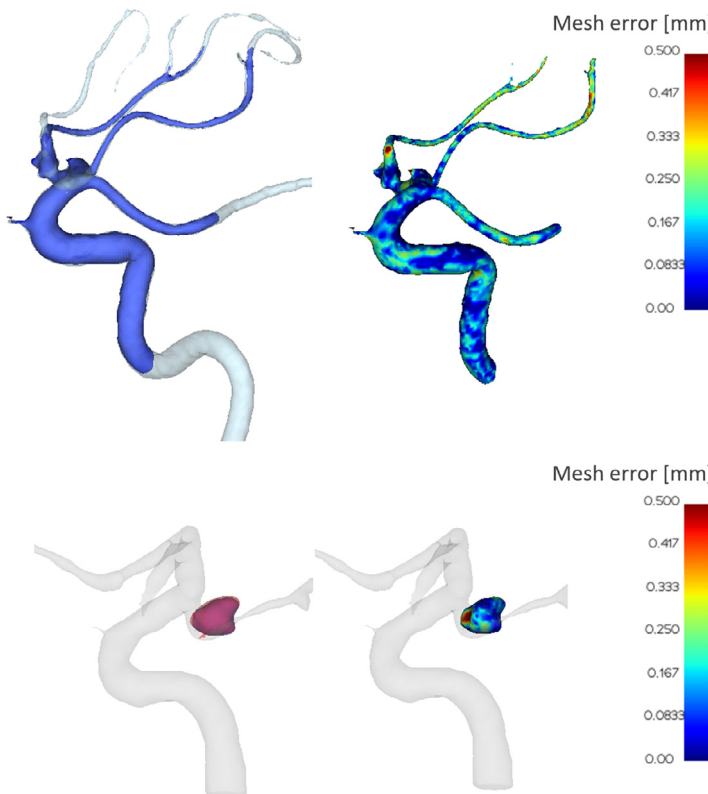


Fig. 12. Surface-to-surface error. Upper left: vessel overlap of ground-truth (blue) and prediction (translucid white). Upper right: surface-to-surface vessel error. Bottom left: aneurysm overlap of ground truth (red) and prediction (orange). Bottom right: aneurysm surface-to-surface error. (For interpretation of the references to colour in this figure legend, the reader is referred to the web version of this article.)

are fed back into the multi-class network to refine the segmentation near the aneurysm (called 'self-refinement'). The improvement in aneurysm segmentation accuracy afforded by these two post-processing steps involving majority voting and self-refinement is also highlighted for the test set in Fig. 10.

Visual comparisons of the maximum intensity projections of segmentations predicted using our approach, and those predicted by state-of-the-art techniques for two samples from the @neurIST test set are presented in Fig. 11. These figures highlight our approach's ability to preserve fine vascular structures greater than its state-of-the-art counterparts. In the @neurIST dataset, ground-truth masks are available only for large vessels near the aneurysm in the second column of Fig. 11. Therefore, for every case, after getting the final segmentation result, we cropped the prediction into a mask with the same size and position as the ground truth. Then the cropped mask is quantitatively evaluated with ground truth. Due to the lack of annotation of small vessels, the image-based as-

essment does not provide the most reasonable evaluation of the segmentation effect. In addition to evaluating segmentation quality using image-based metrics such as Dice, we computed the surface-to-surface distance error between the predicted and ground-truth meshes by reconstructing the former just within the field of view of the corresponding ground-truth mask. The surface-to-surface error metric also provides information regarding the spatial distribution of errors across the anatomical structures of interest, i.e., mapping the vertex-wise nearest neighbor distances between the predicted and ground-truth meshes onto each former vertex (as shown in Fig. 12). Evaluation of surface-to-surface errors in this manner thus provides spatial context to where segmentation errors are incurred and help quantify localized errors, complementing other global image-based metrics (such as Dice) used to evaluate segmentation performance.

Each block of our encoder is dual-path, one for 3D convolution and the other for 2D convolution in multi-view blocks. In

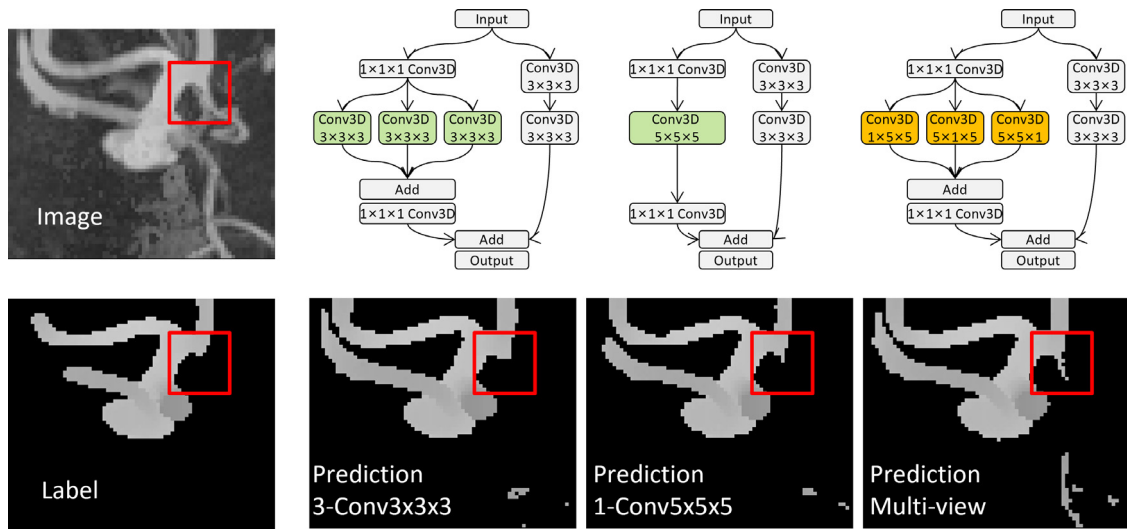


Fig. 13. Comparison of maximum intensity projection between multi-view block (yellow), three conv3D- $3 \times 3 \times 3$ layers, and one conv3D- $5 \times 5 \times 5$ layer. The multi-view block can predict more small vessels even not annotated in the label. (For interpretation of the references to colour in this figure legend, the reader is referred to the web version of this article.)

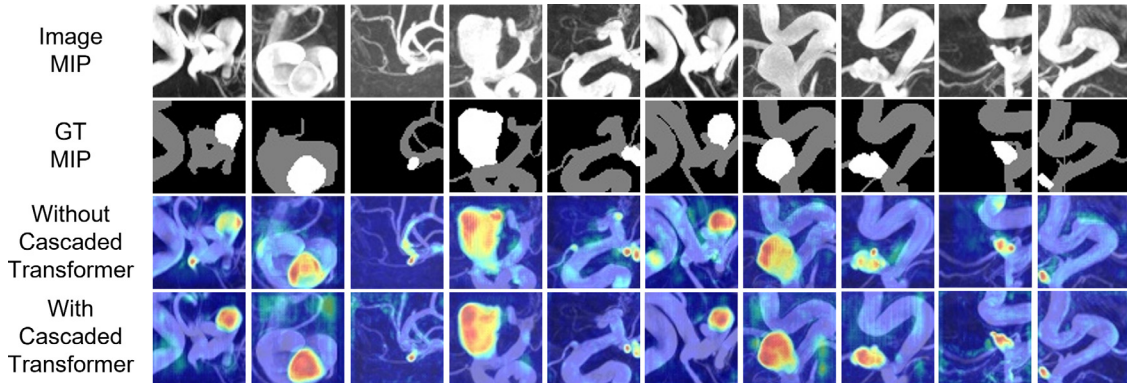


Fig. 14. Visual comparison of attention maps with and without cascaded transformer. The first, second, third, and fourth rows are the image MIPs, vessel and aneurysm segmentation ground truth, attention maps without the cascaded transformer, and attention maps with the cascaded transformer, respectively. As can be seen by comparing each case in the same column, with the cascaded transformer, the model reduces focus on irrelevant context structures like vessel bend and bifurcation.

Fig. 13, to verify that the role of the multi-view block is to provide additional fine features to the 3D convolution backbone pathway rather than adding more parameters, we replaced the three orthogonal 2D convolution layers in the multi-view block with three 3D convolution layers in kernel size 3 or one 3D convolution layer in kernel size 5. The multi-view block has fewer parameters than the other two settings but can mine additional features that are different from the 3D convolution features. Comparing the predictions in the red box, the multi-view block can predict more small vessels even those not annotated on the label. We have also performed an ablation study with and without the cascaded transformer and visualized the attention maps overlaid on the original images, as shown in **Fig. 14**. As can be seen by comparing each case in the same column, with the cascaded transformer, the model reduces focus on irrelevant context structures like vessel bend and bifurcation. Besides, the aneurysm necks are better identified with the attention of the cascaded transformer.

4.2. Quantitative evaluation

Quantitative metrics summarize our approach's segmentation performance and the state-of-the-art, namely, U-Net++, Dual Attention Net, DeepVesselNet, and nnUNet, across all test samples

from the 5-fold cross-validation experiments conducted using the @neurist dataset is presented in **Table 3**. All the quantitative evaluation results were calculated within a bounding box encapsulating the GT labeled region (yellow box in **Fig. 11**). These results indicate that our method consistently outperforms all competing methods in the Dice score, Jaccard index, VS index, and the average surface-to-surface error across the 5fold cross-validation experiments conducted. The statistical significance of the obtained segmentation results was evaluated (using paired-sample Student's t-tests), revealing that our approach achieved significant improvements over the state-of-the-art in terms of Dice and the average surface-to-surface error metrics for both vessels and aneurysms. For vessel segmentation, all methods achieved a Dice score higher than 0.85, indicating that all methods (including ours) were well suited to this task. On the other hand, aneurysm segmentation was more challenging as the target region often constitutes less than 1% of the overall image volume. We found that the state-of-the-art methods investigated in this study failed to perform adequately on this task. nnUNet achieved the best results among the state-of-the-art methods are dedicated pre-processing and post-processing approaches, with a Dice of 0.67 and surface-to-surface error of 1.06 mm. Our approach provided the best aneurysm segmentation performance, achieving a 15% and 0.86 mm improvement over nnUNet in terms of aneurysm Dice and surface-to-surface error.

Table 3
Compare with state-of-the-art on whole @neurIST dataset. 5-fold cross-validation experiments were conducted for each method. The results were calculated in the golden standard area. Our method outperforms other methods on the main evaluation metrics of segmentation and is statistically significant on most items.

Method	U-Net+[15]		Dual Attention Net[16]		DeepVesselNet[17]		mUNet[1]		Ours	
	Vessel	Aneurysm	Vessel	Aneurysm	Vessel	Aneurysm	Vessel	Aneurysm	Vessel	Aneurysm
Dice Similarity Index	0.8982 ± 0.1091	0.5980 ± 0.3398	0.8893 ± 0.1380	0.5949 ± 0.3372	0.8918 ± 0.0968	0.1558 ± 0.2347	0.8687 ± 0.1197	0.6686 ± 0.3190	0.9125 ± 0.0759	0.8163 ± 0.2672
Jaccard Index	0.8271 ± 0.1225	0.5035 ± 0.3216	0.8184 ± 0.1453	0.4993 ± 0.3205	0.8147 ± 0.1174	0.1083 ± 0.1899	0.7820 ± 0.1371	0.5745 ± 0.3058	0.8455 ± 0.0935	0.7486 ± 0.2655
Volume Similarity	0.9461 ± 0.0999	0.6579 ± 0.3372	0.9453 ± 0.0951	0.6634 ± 0.3338	0.9455 ± 0.0740	0.2619 ± 0.2767	0.9131 ± 0.1074	0.7321 ± 0.3072	0.9525 ± 0.0489	0.8693 ± 0.2520
Surface-to-surface error (mm)	0.3441 ± 0.4422	1.1398 ± 2.3495	0.3518 ± 0.4668	1.0623 ± 2.3829	0.4227 ± 0.7354	4.3694 ± 7.4209	0.8903 ± 1.2450	1.0611 ± 2.9100	0.2586 ± 0.3066	0.2021 ± 0.1790
p-value (Dice vs ours)	<0.05	<0.05	<0.05	<0.05	<0.05	<0.05	<0.05	<0.05	/	/
p-value (Surf vs ours)	<0.05	<0.05	<0.05	<0.05	<0.05	<0.05	<0.05	<0.05	/	/

Tables 4 summarizes the results from the ablation study conducted to evaluate the impact of each module included in the proposed multi-class segmentation network on the quality of the predicted vessel and aneurysm segmentation, respectively. The ablation studies which remove modules separately were conducted to verify whether each module contributed positively to the final segmentation performance and determine the importance of different modules. Due to the dataset being partially labeled, the Dice values can not measure unlabeled fine vessels and small aneurysms, so we use surface-to-surface error to measure the performance on labeled parts. Model 1 to Model 5 represent the cases where one module is removed from the final model. The results comparison between ours with Model 1 to Model 5 show that the surface-to-surface error is increased no matter which module is discarded, proving that each adopted technique contributes to the improved accuracy of vessel segmentation. The final model yields the smallest surface-to-surface error in aneurysm segmentation. The absence of certain modules can lead to completely incorrect segmentation results, thus reducing overall segmentation performance on a test set, so each module is essential for aneurysm and vessel segmentation.

We also compared single-class segmentation networks (trained individually for aneurysm and vessel segmentation) with the multi-class network, where identical network architectures were used except for the output layer. Results from this comparison are presented in **Table 5**, which highlights the added advantage of multi-class learning relative to training independent networks for segmenting each structure individually. Our multi-class network significantly outperforms the single-class network for aneurysm average surface-to-surface error (0.2021 vs 0.7051). However, for vessel segmentation, the multi-class network only provided a marginal improvement over the single-class network. Since aneurysms grow on blood vessels, the aneurysm part is also labeled as part of the vessel during training, the learning of vascular features will have a positive effect on the extraction of aneurysm features.

The proposed approach was also trained and evaluated on the public cerebral aneurysm segmentation (CADA-AS) challenge dataset [5]. The segmentation performance of our approach was compared against the best-performing methods in this challenge, 3DResUNet. When comparing these methods, instead of using $128 \times 128 \times 128$ patch size described in the challenge paper, an input patch size of $64 \times 64 \times 64$ was used to analyze and segment the images due to limited computing resources of 1080ti GPU card. Results summarizing aneurysm segmentation performance on test data from the CADA-AS challenge are presented in **Table 6**. Since the data is fully labeled, we add the Dice Similarity Index in addition to surface-to-surface error. These results indicate that our approach outperforms 3DResUNet, in terms of both metrics.

A key aspect of quantitative analysis of cerebral aneurysms, either in assessing cerebral hemodynamics or aneurysm rupture risk, is the precise characterization of their morphological properties. Hence, besides evaluating aneurysm segmentation quality using standard image-based and mesh-based metrics, we compared our approach with state-of-the-art segmentation approaches to preserve each segmented aneurysm's maximum diameter and volume relative to the ground truth. The Bland–Altman plots [20–22] in **Fig. 15**, summarize the average errors between predicted and ground-truth measurements for aneurysm maximum diameter and volume and their corresponding 95% confidence intervals for each method investigated. These results indicate no apparent bias in our model's ability to preserve critical morphological characteristics of aneurysms, unlike DeepVesselNet, for example. Additionally, the average errors incurred by our approach regarding the ground-truth measurements are consistently lower than all competing approaches.

Table 4

Ablation study. These models are in the same pre-processing and post-processing method (proposed). The experiments remove different modules separately. Due to the dataset being partially labeled, the Dice values can not measure unlabeled fine vessels and small aneurysms, so we use surface-to-surface error to measure the performance on labeled parts.

Model	Surface-to-surface error (mm)					
	Model 1	Model 2	Model 3	Model 4	Model 5	Ours
Absent module Modules	Nested Block	Multi-view	Transformer	L-Down	Wide	
	UNet Multi-view	U-Net+ Transformer	U-Net+ Multi-view	U-Net+ Multi-view	U-Net+ Multi-view	U-Net+ Multi-view
	Transformer	L-Down Wide	L-Down Wide	Transformer Wide	Transformer	Transformer
	L-Down Wide			L-Down	L-Down	L-Down Wide
Vessel	0.3127 ± 0.2462	0.3329 ± 0.3466	0.3327 ± 0.3258	0.3286 ± 0.2876	0.3137 ± 0.2536	0.2586 ± 0.3066
Aneurysm	0.4630 ± 1.0255	1.0878 ± 4.2235	0.3658 ± 0.7354	0.2738 ± 0.3327	0.3921 ± 0.6521	0.2021 ± 0.1790

Table 5

Comparison between single-class and multi-class. The pre-processing and post-processing of the experiments are the same.

Training type	Single-class		Multi-class	
	Anatomical Structure	Aneurysm	Vessel	Aneurysm
Surface-to-surface error (mm)		0.7051 ± 0.9031	0.3024 ± 0.1641	0.2021 ± 0.1790
				0.2586 ± 0.3066

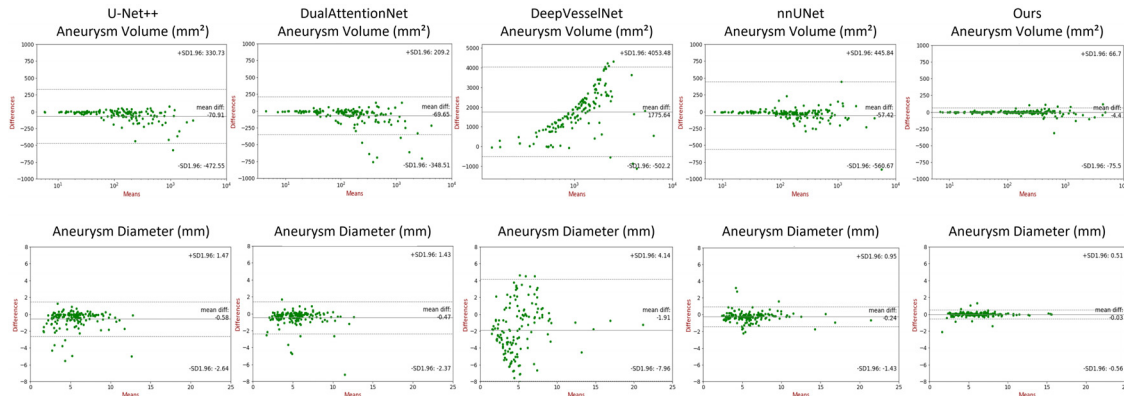


Fig. 15. Bland–Altman plots: Mean and difference of aneurysm radius and volume between ground-truth and predictions. Our method has a more compact distribution. In terms of clinical criteria, our predictions are much closer to the ground truth.

Table 6

Compare our method on the cerebral aneurysm segmentation (CADA-AS) dataset with its champion methods. All models were retrained and tested on this single-class dataset.

CADA-AS	3DResUNet	Ours
Dice Similarity Index	0.7464 ± 0.1379	0.8737 ± 0.0747
Surface-to-surface error (mm)	0.4102 ± 0.3924	0.3817 ± 0.3984

Table 8

Average prediction time for one image volume.

Step	Time
Step1: Preprocessing	5 s
Step2: Multi-class Segmentation	45 s
Step3: Post-processing	46 s
Total	96 s

Table 7

False-positive prediction rate for the aneurysm with or without post-processing.

Post-processing	False-Positive Rate	Dice Similarity Index
✗	65 / 223	0.6432 ± 0.3333
✓	23 / 223	0.8163 ± 0.2672

In addition, Table 7 has included the false-positive rate and Dice score for the aneurysm segmentation before and after applying the post-processing technique. As can be seen, the proposed post-processing can fix 42 over-segmented aneurysm cases while improving the overall Dice for aneurysm by 15%. Table 8 illustrated the average prediction time for one volumetric image generated by the proposed framework in different steps. The proposed method uses an average of 1.5 min to process an image volume for vessel and aneurysm segmentation.

5. Discussion

This paper presented a multi-class convolution neural network and a 3D patch-based pipeline for cerebrovascular and aneurysm segmentation on 3DRA images. Vessel and aneurysm segmentation in 3DRA is very challenging due to the small percentage of vessels and aneurysms and the interference of the skull. Compared to standardized, homogeneous data, clinical data exhibit more noise, heterogeneous, diverse appearance and resolution, making this task more challenging. With severe class imbalance, automatic segmentation methods struggle to extract the complete contextual and local information from images. To alleviate those issues, our proposed network has a transformer block sensitive to small-scale features, multi-view blocks sensitive to continuous features, the learnable downsample block that prevents subtle features from being lost, and wide blocks that expand local perceptual fields. Besides, the dedicated post-processing methods of majority voting

and self-refinement can effectively suppress the over-segmentation of the clinical aneurysm, enhancing the entire pipeline's clinical robustness.

5.1. Class imbalance

In whole brain tissue, the percentage of blood vessels is less than 6% [47], and the proportion of aneurysms is less than that of vessels. Hence, U-Net++ and Dual Attention Net are potent models that retain rich intermediate features and focus more on critical target information. However, these models can only capture the main vessels and obvious aneurysms. Still, these models lose subtle features during the convolution operation, viz., small aneurysms whose diameter is less than 10 mm. Our method designed multi-view blocks and wide blocks for the class imbalance problem by extracting additional information to complement the backbone network feature. These blocks can extract continuous information through cascade and parallel low-dimensional convolution layers with large kernels. We also exploited a transformer block at the end of the encoder to enlarge the proportion of target features. In Table 4, after adding different new modules, the segmentation of both aneurysms and vessels is improved, which also verifies that the proposed modules positively affect the final segmentation results. In addition, in order to reduce the proportion of negative samples and thus make the training converge, when preparing the training patches, we select the patches around the aneurysm as input instead of feeding all patches obtained after cropping the data to a model. This can increase the proportion of aneurysms and vessels in a single patch.

5.2. Inter-class separability

Aneurysm segmentation usually suffers from inter-class interference. Due to the prior knowledge that all aneurysms grow on vessels while extracting the vessel features, the deep network also extracts and enhances more potential aneurysm features near the vessels. Without proper guidance of vessel features in multi-class, the single-class model may segment brain tissue or noise area into aneurysms. The multi-class learning brings a huge boost to aneurysm segmentation. From Table 5, multi-class aneurysm segmentation surface-to-surface error improved by 0.5 mm over single-class.

5.3. Inter-institutional data variability

Our data were obtained from four institutions. While data from different sources are all from the same modality, viz. 3DRA images, there are large differences in image appearance, intensity distribution, resolution and aneurysm size (Fig. 8). This poses a great challenge to the robustness of the model. Automatic models such as nnUNet and Deep Vessel Net use pre-processing and post-processing methods like patch-based learning and Gaussian standardization. These methods perform well on challenging datasets with good pre-processing. However, these segmentation methods lead to aneurysm over-segmentation in clinical data. To improve clinical robustness, we propose majority voting, which returns the prediction most like an aneurysm to find the exact aneurysm localization. Then, self-refinement further corrects the aneurysm contour details. Through our experiment, we found the necessity of the post-processing step in our current framework setting because 1) it helps to mitigate the over-segmentation of aneurysms due to the similarity of closed vessels in patch boundary to aneurysms in morphology; 2) it avoids to use of larger patch sizes that would further aggregate the data imbalance and result in performance degradation in aneurysm segmentation.

Table 9

Compare our method on aneurysm segmentation success rate (surface-to-surface error smaller than 1 mm) with SOTA methods.

Methods	Aneurysm segmentation success rate
U-Net+	150 / 223
Dual Attention Net	152 / 223
DeepVesselNet	144 / 223
nnUNet	173 / 223
Ours	190 / 223

The fourth column in Fig. 2 top shows majority voting returns the maximum prediction probability and effectively suppresses over-segmentation. The later self-refinement makes the aneurysm details more accurate. To validate the robustness of the pipeline, besides clinical data, we also evaluated our method on the CADA-AS competition dataset (c.f. Table 6). Our segmentation method yielded results close to the championship method [19]. For in silico clinical trials, the accuracy of aneurysm localization is as important as Dice and Surface-to-surface error. Table 9 shows the success rate of aneurysm prediction for each algorithm. Only cases with a surface-to-surface error of less than 1 mm were defined as success cases, which means that such cases have accurate localization and segmentation. In 223 clinical cases from four different data centers, our method yielded accurate aneurysm prediction in 190 cases. However, among other methods, the best is nnUNet which only got 173 success cases. In addition, our method outperforms these comparative methods in terms of clinical indicators such as aneurysm diameter and volume. The Bland–Altman plots in Fig. 15 demonstrate that our method yields a difference of $-0.03 \pm 0.54 \text{ mm}$ and $-4.4 \pm 71.1 \text{ mm}^2$ in aneurysm diameter and volume with ground truth, which is the smallest (best) compared to other methods.

Although our method achieved improved performance for automatic segmentation of vessels and aneurysms, due to the limitation of incomplete labeling of 3DRA datasets, the wrongly labeled background pixels for missing vessels could interfere with the overall training process. Thus, future work would involve leveraging semi-supervised schemes to enhance the learning of unlabelled parts, e.g., relabelling the missing annotations during the training process by introducing pseudo-labels. Meanwhile, since there are still a large number of unlabelled 3DRA image data in our clinical dataset, the joint training of the labeled 3DRA data and unlabeled data under a semi-supervised setting is also a worthy direction of research.

6. Conclusion

This work proposed a 3D patch-based multi-class model for vessel and aneurysm segmentation on 3DRA images. The proposed approach addressed class imbalance problems and inter-class interference problems in multi-class segmentation. Experimental results showed that the proposed method outperformed several popular state-of-the-art approaches for tackling similar challenges, such as U-Net++, DeepVesselNet, and nnUNet. This work aims to alleviate class imbalance and inter-class interference, which are common and challenging problems in cerebrovascular and aneurysm segmentation. The deliberately designed network architectures such as the cascaded transformer, multi-view block, and wide block as well as the proposed post-processing strategies of the majority voting and self-refinement contribute positively to mining vascular and aneurysm features through the proposed end-to-end trainable network. The aforementioned issues are also present in brain MRA and CTA when it comes to cerebrovascular and aneurysm segmentation. The proposed model is generic and can be applied to mitigate the issues of class imbalance and inter-class interference in

brain MRA and CTA, promising to facilitate accurate clinical analyses. The systematic evaluation of the model performance on other modalities would be the scope of future work.

Declaration of Competing Interest

The authors whose names are listed immediately below certify that they have NO affiliations with or involvement in any organization or entity with any financial interest (such as honoraria; educational grants; participation in speakers' bureaus; membership, employment, consultancies, stock ownership, or other equity interest; and expert testimony or patent-licensing arrangements), or non-financial interest (such as personal or professional relationships, affiliations, knowledge or beliefs) in the subject matter or materials discussed in this manuscript.

The authors whose names are listed immediately below report the following details of affiliation or involvement in an organization or entity with a financial or non-financial interest in the subject matter or materials discussed in this manuscript. Please specify the nature of the conflict on a separate sheet of paper if the space below is inadequate.

Acknowledgments

AFF acknowledges the support of the Royal Academy of Engineering under the RAEEng Chair in Emerging Technologies (CIELT1919/19) scheme. AFF acknowledges seminal funding from the European Commission to @neurIST (FP6-2004-IST-4-027703) and the @neurIST Consortium. The European Commission funded AFF via InSilc (H2020-SC1-2017-CNECT-2-777119). We also want to thank anonymous reviewers for their constructive comments that have made our presentation and testing complete, improving the quality of our work.

References

- [1] F. Isensee, P.F. Jaeger, S.A.A. Kohl, et al., nnU-Net: a self-configuring method for deep learning-based biomedical image segmentation, *Nat. Methods* 18 (2) (2021) 203–211.
- [2] M.V. Orlov, P. Hoffmeister, G.M. Chaudhry, et al., Three dimensional rotational angiography of the left atrium and esophagus—a virtual computed tomography scan in the electrophysiology lab? *Heart Rhythm* 4 (2007) 37–43.
- [3] J. Ector, S. De Buck, D. Nuyens, et al., Adenosine-induced ventricular asystole or rapid ventricular pacing to enhance three-dimensional rotational imaging during cardiac ablation procedures, *Europacce* 11 (2009) 751–762.
- [4] T.J.R. De Potter, G. Bardají, A. Viggiano, et al., Three-dimensional rotational angiography as a periprocedural imaging tool in atrial fibrillation ablation, *Arrhythmia Electrophysiol. Rev.* 3 (3) (2014) 173.
- [5] A. Hennemuth, in: *Cerebral Aneurysm Detection: First Challenge, CADA 2020*, Held in Conjunction with MICCAI 2020, Lima, Peru, October 8, 2020, Proceedings, Springer Nature, 2021.
- [6] M. Livne, J. Rieger, O.U. Aydin, et al., A U-Net deep learning framework for high performance vessel segmentation in patients with cerebrovascular disease, *Front. Neurosci.* 13 (2019) 97.
- [7] A. Hilbert, V.I. Madai, E.M. Akay, et al., BRAVE-NET: fully automated arterial brain vessel segmentation in patients with cerebrovascular disease, *Front. Artif. Intell.* (2020) 78.
- [8] C. Guo, M. Szemenyei, Y. Yi, et al., SA-UNet: spatial attention U-Net for retinal vessel segmentation, in: *2020 25th International Conference on Pattern Recognition (ICPR)*, IEEE, 2021, pp. 1236–1242.
- [9] R. Shahzad, L. Pennig, L. Goertz, et al., Fully automated detection and segmentation of intracranial aneurysms in subarachnoid hemorrhage on CTA using deep learning, *Sci. Rep.* 10 (1) (2020) 1–12.
- [10] K. Kamnitsas, E. Ferrante, S. Parisot, et al., DeepMedic for brain tumor segmentation, in: *International Workshop on Brainlesion: Glioma, Multiple Sclerosis, Stroke and Traumatic Brain Injuries*, Springer, Cham, 2016, pp. 138–149.
- [11] N.F. Dengler, V.I. Madai, J. Wuerfel, et al., Moyamoya vessel pathology imaged by ultra-high-field magnetic resonance imaging at 7.0 T, *J. Stroke Cerebrovasc. Dis.* 25 (6) (2016) 1544–1551.
- [12] Q. Wang, W. Wang, Z. Fei, et al., Simulation of blood flow in intracranial ICA-PComa aneurysm via computational fluid dynamics modeling, *J. Hydromech.* 21 (5) (2009) 583–590.
- [13] T.R. Patel, N. Paliwal, P. Jaiswal, et al., Multi-resolution CNN for brain vessel segmentation from cerebrovascular images of intracranial aneurysm: a comparison of u-net and deepmedic, *Medical Imaging 2020: Computer-Aided Diagnosis*, 113142W, Vol. 11314, International Society for Optics and Photonics, 2020.
- [14] O. Ronneberger, P. Fischer, T. Brox, U-Net: convolutional networks for biomedical image segmentation, in: *International Conference on Medical Image Computing and Computer-Assisted Intervention*, Springer, Cham, 2015, pp. 234–241.
- [15] Z. Zhou, M.M.R. Siddiquee, N. Tajbakhsh, et al., UNet++: redesigning skip connections to exploit multiscale features in image segmentation, *IEEE Trans. Med. Imaging* 39 (6) (2019) 1856–1867.
- [16] J. Fu, J. Liu, H. Tian, et al., Dual attention network for scene segmentation, in: *Proceedings of the IEEE/CVF Conference on Computer Vision and Pattern Recognition*, 2019, pp. 3146–3154.
- [17] G. Tetteh, V. Efremov, N.D. Forkert, N. in, et al., DeepVesselNet: vessel segmentation, centerline prediction, and bifurcation detection in 3-D angiographic volumes, *Frontiers* 14 (2020) 1285.
- [18] S. Benkner, A. Arbona, G. Berti, et al., @neurIST: infrastructure for advanced disease management through integration of heterogeneous data, computing, and complex processing services, *IEEE Trans. Inf. Technol. Biomed.* 14 (6) (2010) 1365–1377.
- [19] M. Ivantsits, L. Goubergrits, J.M. Kuhnigk, et al., Cerebral aneurysm detection and analysis challenge 2020 (CADA), in: *International workshop on Cerebral Aneurysm Detection*, Springer, Cham, 2020, pp. 3–17.
- [20] K. Dewitte, C. Fierens, D. Stockl, et al., Application of the Bland–Altman plot for interpretation of method-comparison studies: a critical investigation of its practice, *Clin. Chem.* 48 (5) (2002) 799–801.
- [21] J.M. Bland, D.G. Altman, Measuring agreement in method comparison studies, *Stat. Methods Med. Res.* 8 (2) (1999) 135–160.
- [22] J.M. Bland, D.G. Altman, Statistical methods for assessing agreement between two methods of clinical measurement, *Lancet* 327 (8476) (1986) 307–310.
- [23] M.K. Kalra, P. Dang, S. Singh, et al., In-plane shielding for CT: effect of off-centering, automatic exposure control and shield-to-surface distance, *Korean J. Radiol.* 10 (2) (2009) 156–163.
- [24] D.P. Kingma, J. Ba, Adam: a method for stochastic optimization, 2014, *arXiv preprint arXiv:1412.6980*.
- [25] S. Jadon, A survey of loss functions for semantic segmentation, in: *2020 IEEE Conference on Computational Intelligence in Bioinformatics and Computational Biology (CIBCB)*, IEEE, 2020, pp. 1–7.
- [26] R. Li, M. Li, J. Li, et al., Connection sensitive attention u-net for accurate retinal vessel segmentation, 2019, *arXiv preprint arXiv:1903.05558*.
- [27] L.C. Chen, Y. Yang, J. Wang, et al., Attention to scale: scale-aware semantic image segmentation, in: *Proceedings of the IEEE Conference on Computer Vision and Pattern Recognition*, 2016, pp. 3640–3649.
- [28] Z. Huang, X. Wang, L. Huang, et al., CCNet: criss-cross attention for semantic segmentation, in: *Proceedings of the IEEE/CVF International Conference on Computer Vision*, 2019, pp. 603–612.
- [29] H. Li, P. Xiong, J. An, et al., Pyramid attention network for semantic segmentation, *arXiv preprint arXiv:1805.10180* (2018).
- [30] A.A. Taha, A. Hanbury, Metrics for evaluating 3D medical image segmentation: analysis, selection, and tool, *BMC Med. Imaging* 15 (1) (2015) 1–28.
- [31] A. Kolesnikov, A. Dosovitskiy, D. Weissenborn, et al., An image is worth 16x16 words: transformers for image recognition at scale, 2021.
- [32] T. Sugahara, Y. Korogi, K. Nakashima, et al., Comparison of 2D and 3D digital subtraction angiography in evaluation of intracranial aneurysms, *Am. J. Neuroradiol.* 23 (9) (2002) 1545–1552.
- [33] R. Axionnot, S. Bracard, X. Ducrocq, et al., Intracranial aneurysms: clinical value of 3D digital subtraction angiography in the therapeutic decision and endovascular treatment, *Radiology* 218 (3) (2001) 799–808.
- [34] P.M. White, J.M. Wardlaw, V. Easton, Can noninvasive imaging accurately depict intracranial aneurysms? a systematic review, *Radiology* 217 (2) (2000) 361–370.
- [35] W.J. van Rooij, M.E. Sprengers, A.N. de Gast, et al., 3D rotational angiography: the new gold standard in the detection of additional intracranial aneurysms, *Am. J. Neuroradiol.* 29 (5) (2008) 976–979.
- [36] S. Tanoue, H. Kiyoze, H. Kenai, et al., Three-dimensional reconstructed images after rotational angiography in the evaluation of intracranial aneurysms: surgical correlation, *Neurosurgery* 47 (4) (2000) 866–871.
- [37] S. Moccia, E. De Momi, S. El Hadji, et al., Blood vessel segmentation algorithm—s-review of methods, datasets and evaluation metrics, *Comput. Methods Programs Biomed.* 158 (2018) 71–91.
- [38] A. Firouzian, R. Manniesing, Z.H. Flach, et al., Intracranial aneurysm segmentation in 3D CT angiography: method and quantitative validation with and without prior noise filtering, *Eur. J. Radiol.* 79 (2) (2011) 299–304.
- [39] F. Taher, A. Soliman, H. Kandil, et al., Accurate segmentation of cerebrovasculature from TOF-MRA images using appearance descriptors, *IEEE Access* 8 (2020) 96139–96149.
- [40] M. Russ, R. O'Hara, S.V.S. Nagesh, et al., Treatment planning for image-guided neuro-vascular interventions using patient-specific 3D printed phantoms, in: *Medical Imaging 2015: Biomedical Applications in Molecular, Structural, and Functional Imaging*, Vol. 9417, International Society for Optics and Photonics, 2015, p. 941726.
- [41] J.R. Cebral, F. Mut, D. Sforza, et al., Clinical application of image-based CFD for cerebral aneurysms, *Int. J. Numer. Method Biomed. Eng.* 27 (7) (2011) 977–992.
- [42] N. Chalouhi, B.L. Hoh, D. Hasan, Review of cerebral aneurysm formation, growth, and rupture, *Stroke* 44 (12) (2013) 3613–3622.

- [43] A. Sarrami-Foroushani, T. Lassila, M. MacRaild, et al., In-silico trial of intracranial flow diverters replicates and expands insights from conventional clinical trials, *Nat. Commun.* 12 (1) (2021) 1–12.
- [44] M. Hernandez, A.F. Frangi, Non-parametric geodesic active regions: method and evaluation for cerebral aneurysms segmentation in 3DRA and CTA, *Medical* 11 (3) (2007) 224–241.
- [45] H. Bogunović, J.M. Pozo, M.C. Villa-Uriol, et al., Automated segmentation of cerebral vasculature with aneurysms in 3DRA and TOF-MRA using geodesic active regions: an evaluation study, *Med. Phys.* 38 (1) (2011) 210–222.
- [46] M. Hernandez, A.F. Frangi, Geodesic active regions using non-parametric statistical regional description and their application to aneurysm segmentation from CTA, in: International Workshop on Medical Imaging and Virtual Reality, Springer, Berlin, Heidelberg, 2004, pp. 94–102.
- [47] A. William, Copen, H. Michael, Lev and Otto Rapalino, *Handbook of Clinical Neurology*. Chapter 6 – Brain Perfusion: Computed Tomography and Magnetic Resonance Techniques, Elsevier, 2016, pp. 117–135.
- [48] K. Golshani, A. Ferrell, A. Zomorodi, et al., A review of the management of posterior communicating artery aneurysms in the modern era, *Surg. Neurol. Int.*, 2010, p. 1.
- [49] C. Sudre, W. Li, T. Vercauteren, S. Ourselin, M. Jorge Cardoso, Generalised dice overlap as a deep learning loss function for highly unbalanced segmentations, in: Deep Learning in Medical Image Analysis and Multimodal Learning for Clinical Decision Support, Springer, Cham, 2017, pp. 240–248. Sep 14
- [50] V.N. Dang, F. Galati, R. Cortese, et al., Vessel-CAPTCHA: an efficient learning framework for vessel annotation and segmentation, *Med. Image Anal.* 75 (2022) 102263.